ISSN 0038-0946, Solar System Research, 2022, Vol. 56, No. 3, pp. 135–144. © Pleiades Publishing, Inc., 2022.
Russian Text © The Author(s), 2022, published in Astronomicheskii Vestnik, 2022, Vol. 56, No. 3, pp. 147–157.

Geological Details of the Main Landing Ellipses of *Luna-25*

S. S. Krasilnikov[a], *, A. S. Krasilnikov[a], and M. A. Ivanov[a]

[a] *Vernadsky Institute of Geochemistry and Analytical Chemistry, Russian Academy of Sciences, Moscow, Russia*

**e-mail: krasilnikovruss@gmail.com*

Received July 20, 2021; revised October 20, 2021; accepted October 26, 2021

Abstract—The work carried out a comprehensive analysis of engineering and scientific requirements within the main landing ellipses of the *Luna-25* expedition. To detail the landing ellipses, data on the conditions of the Earth's visibility, illumination, critical slopes and cratering, in combination with the geological structure and the presence of hydrogen-containing components in the soil, were considered. Within the ellipses, areas with high, medium, and low engineering constraints on the landing and operation of the descent vehicle were identified. Possible sources of matter accumulated in different locations of the landing ellipses are estimated. These data are important for the interpretation of the soil analysis results at the landing site of the descent vehicle.

Keywords: *Luna*, *Luna-Glob*, *Luna-25*, landing sites

DOI: 10.1134/S0038094622020058

INTRODUCTION

The size of the previously selected main landing ellipses 1 (68.773° S, 21.21° E), 4 (68.648° S, 11.553° E) and 6 (69.545° S, 43.544° E) of the *Luna-25* expedition is 15 × 30 km (Djachkova et al., 2017). The internal structure of ellipses is heterogeneous, both from a geological and an engineering point of view (Ivanov et al., 2018) and, therefore, within the ellipses there are more and less safe landing sites with the potential for sampling the regolith of different geological complexes.

The landing site must have a detailed geological description, which would make it possible to reconstruct the history of the formation of the tested geological complexes and to determine the sources of their matter. This knowledge plays a decisive role in the interpretation of the results of analyses that the lander will carry out on the surface. The purpose of this work is a general engineering and geological detailing of the previously selected ellipses, with the determination of the scientific potential of geological and geomorphological units and the search for possible sources of matter accumulated in potential landing sites.

INITIAL DATA AND RESEARCH METHODS

The work uses the results of previous studies, (Ivanov et al., 2018; Krasilnikov et al., 2018, 2021), as well as new data for selected ellipses obtained using LEND instruments (Sanin et al., 2017) and Diviner (Paige et al., 2010) installed on the *LRO* (Lunar Reconnaissance Orbiter) orbiter. For engineering–geological detailing of the ellipses, a detailed geological map was compiled for the landing sector (65°–75° S and 0°–52° E) at a scale of 1 : 300000 and maps at a scale of 1 : 100000 on landing ellipses of the *Luna-25* expedition. Geological analysis of the landing area was based on mosaics of images of wide-angle (WAC, Wide Angle Camera) and narrow-angle (NAC, Narrow Angle Camera) cameras of the *LRO* spacecraft with a spatial resolution of 100 and 0.5–1 m/px, respectively (Robinson et al., 2010), and also on a digital elevation model (DEM) with a resolution of 60 m/px, built according to the LOLA altimeter (Lunar Orbiter Laser Altimeter; Smith et al., 2010). For the ellipses, geological sections were built to estimate the power of the ejection craters overlapping the study region. NAC images were also used to determine the power of small crater ejections (less than 1 km in diameter), to calculate the density of small craters and rockiness of the surface.

Geological sections through the landing ellipses were built using laser altimetry data with LOLA, model emission power and geological maps compiled in this study based on works (Ivanov et al., 2018) and (Krasilnikov et al., 2021). The data of the morphological structure of the surface and the nature of the distribution of the ejected material were taken into account. For better visualization of the sections, the ratio of the horizontal and vertical scales was 1 : 5. The emission power was calculated for all craters/basins (impact structures with a diameter of more than 300 km) affecting the geological structure of the landing ellipses. The power was calculated using the model of Housen et al. (1983) for large craters with a diameter of more than 45 km and the Sharpton (2014) model for smaller craters. In the model of Housen et al. (1983)

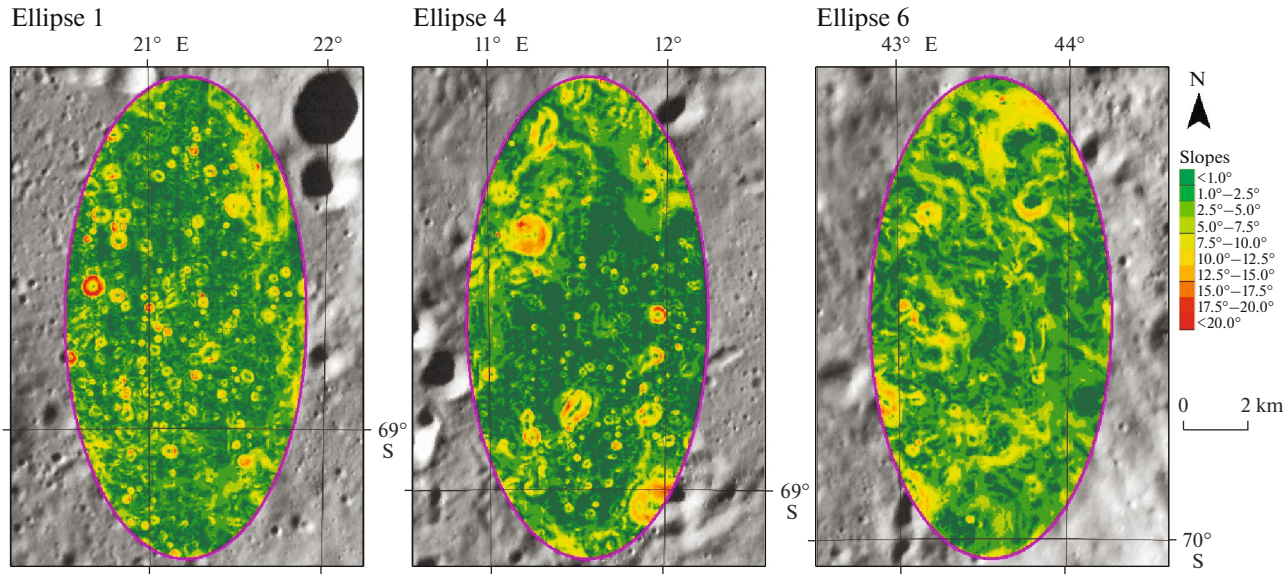

Fig. 1. Surface inclination based on 60 m/pix LOLA data.

the radial decrease in the emission power is described by the formula:

$$T = 0.0078 \times R(r/R)^{-2.61},$$

and in the model of Sharpton (2014):

$$T = 3.95(\pm 1.19) R^{0.399}(r/R)^{-3}.$$

The model of Fassett et al. (2011), which describes the change in radial power by the formula:

$$T = 2900(\pm 300) R \times (r/R)^{-2.8(\pm 0.5)},$$

for all formulas R is the radius of the crater/basin, and r is the distance from the center of the crater.

The emission power was calculated along the radius from the side of the crater/basin with a step of 5 km. When constructing the section, deposits of small craters were also taken into account, which eject and move material from under the overlying layers on a local scale (hundreds of meters to kilometers).

ENGINEERING REQUIREMENTS

Illumination of the surface and line of sight from the Earth are among the important engineering requirements for the landing site of the descent vehicle. The illumination of the device will allow it to generate enough energy for its operation on the surface, and the line of sight from the Earth will allow establishing stable radio communications for data transmission. These requirements are considered in more detail in the work (Djachkova et al., 2017). In our article, we used the averaged values of the surface illumination by the Sun and visibility from the Earth for the year (Mazarico et al., 2011), obtained from the LOLA data. The areas with high limits are pixels with an illumination value of ≤40% per unit time, areas with an average limit correspond to an illumination of 40–45%, and with illumination >45%, the territory is considered to be a low restriction area. A similar classification has been applied to line-of-sight data from the Earth: ≤95%, high limits; 95–99%, medium; and 100%, low.

To determine the slopes of the surface, LOLA data with a resolution of 60 m (Fig. 1) and the shadow method were used, which makes it possible to estimate the incidence of slopes on a base comparable to the horizontal dimensions of the descent vehicle of 3.5 m (Abdrakhimov et al., 2015; Krasilnikov et al., 2018). Sloped surfaces <7° (at a maximum base of 60 m) have low limits, with 7°–10° slopes medium, and >10° high.

GEOLOGICAL STRUCTURE OF THE RESEARCH SECTOR

To reconstruct the geological history in the landing sector of the *Luna-25* expedition, its geological mapping was carried out on a scale of 1 : 300000, the results of which were compared with earlier maps: with a global geological map at a scale of 1 : 5000000 (Wilhelms, 1972) and with a geological map of the landing sector at a scale of 1 : 500000 (Ivanov et al., 2018). Our geological map of the landing sector covers an area between 65°–75° S and 0°–52° E and presents a fragment of a regional geological map of the Moon's south pole, which is being prepared for publication.

Impact cratering is the dominant factor in the renewal of the lunar surface. The main episode of this renewal in the southern polar region is associated with the formation of the South Pole, the Aitken (SPA)

basin more than four billion years ago (Hiesinger et al., 2012). The pre-Nectarian craters Boguslawsky, Boussingault, Manzinus and Simpelius (pNc), the Nectarian crater (Nc) Boussingault A, and the Imbrian craters Moretus (Ic1) and Schomberger (Ic2) formed on the cover of the basin's emissions. The main part of the studied region (Fig. 2) is covered by ejections from the crater Moretus (Lower Imbrian Age, 3.76 ± 0.03 Ga) and Schomberger (Upper Imbrian Age, 3.66 ± 0.04 Ga).

The stratigraphic age on the regional map (Fig. 2) and the ellipse map (Figs. 3–5) is shown in capital letters and corresponds to the classification Wilhelms (1972). The map shows the sediments of the pre-Nectarian (pN), Nectarian (N), Imbrian and Eratosthenian (E) Ages. The Imbrian Age has been divided into the Lower Imbrian (I1) and Upper Imbrian (I2). Lowercase subscripts after the age indicate the type of surface: "c," the inner part of the crater; "se," the solid cover of secondary ejections from the crater; and "sc," the chains and fields of secondary craters. The main geological and geomorphological divisions: "rp," the rough cratered surface of undetermined age; "sp," the flat surface of a plain of undetermined age; and "cl," landslides, mainly on the slopes of craters.

GEOLOGICAL STRUCTURE OF LANDING ELLIPSES AND PRESENCE OF HYDROGEN IN THE GROUND

In our work, the geological maps of the main landing ellipses were published earlier (Ivanov et al., 2018). The indexes on the ellipse map correspond to the classification described above. After the stratigraphic age and surface type, geological and geomorphological subdivisions are indicated on the ellipse map in accordance with the classification proposed in (Krasilnikov et al., 2021). For the considered ellipses, subdivisions were allocated: "pc" for a cratered gently undulating plain with a medium or high density of small (up to 1000 m in diameter) craters; "rp," a hilly-depression plain with a low to medium density of craters; "sh," gently sloping hills, with insignificant elevation differences and a low or medium density of craters; "c," medium-sized craters (from one to several kilometers in diameter), for which an ejection zone can be identified.

Surface rockiness was assessed by comparative analysis of Diviner radiometer data and LROC NAC images. Bandfield et al. (2011) built a mosaic of images on the rockiness of the surface based on Diviner data. The presence of stones within a pixel is indicated by an increase in the thermal inertia of more than 1570 J m^{-2} K^{-1} $s^{-1/2}$ at 200 K. Analysis of the mosaic by the main ellipses showed low rockiness values with a maximum of 0.02% (percentage of the surface with stones 0.5–1 m in diameter from the area of one pixel of the Diviner survey, 237 m^2). Analysis of LROC NAC images also did not reveal significant concentrations of rocky material on the surface (Ivanov et al., 2018). An increase in the number of stones is characteristic of fresh steep craters with surface slopes of more than 10°, which is already a limiting engineering factor, therefore, it is not considered separately in this work.

The main landing ellipses of the *Luna-25* expedition have higher values of the water equivalent of hydrogen in comparison with the rest of the ellipses. Average WEH values are: ellipse 1 (0.13 ± 0.01 wt %, hereinafter 1σ), ellipse 4 and 6 (0.12 ± 0.01 wt %). The spatial distribution of WEH within the ellipses is uneven, for ellipse 1 and 6 there is a gradual increase in values to the north and northeast, respectively, and for ellipse 4, higher values are observed in its southwestern part (Figs. 3–5).

Ellipse 1 (68.77° S, 21.21° E) is located on an intercrater plain formed by the ejecta of craters Manzinus and Simpelius A, presumably pre-Nectarian (pNec) in age (Fig. 3). Within the ellipse, three main geological subdivisions have been distinguished:

(1) A relatively flat cratered plain of Lower Imbrian age, occupying 70.5% of the ellipse (Isc1pc). The plain was formed by ejections from the Manzinus crater with traces of secondary craters from the crater Mutus B (pNec), subsequently overlapped by ejections from the Moretus crater (Isc1). The absolute model age of the plain, estimated from the frequency-size distribution of impact craters, is ~3.82 ± 0.02 Ga (Ivanov et al., 2018). For this unit, an increase in the values of the water equivalent of hydrogen to 0.13–0.14 wt % is observed in the central part of the ellipse, and the average value for the entire unit is 0.13 ± 0.01 wt %. The area with high restrictions for the landing and operation of the descent vehicle in this subdivision is 4.5% of its total area, and with average restrictions, 6.3%.

(2) A slightly sloping hilly-depression surface with elongated ridges and depressions of the Upper Imbrian age (Isc2rp) is located in the eastern part of the ellipse and occupies 21.1% of its surface. The plain rests on a pre-Nectarian basement and is partially overlapped by the Upper Imbrian deposits of the Manzinus E crater and an unnamed crater to the northwest of the ellipse. The absolute model age of the plain is ~3.62 ± 0.02 Ga (Ivanov et al., 2018). The average WEH value is 0.13 ± 0.01 wt %. The area with high limits within this subdivision is 4.6%, and with low limits, 11.3%.

(3) A crater 1.4 km in diameter and its Upper Imbrian ejections are located in the western part of the ellipse (Ic2) and occupy 8.4% of its area. The average WEH associated with the crater is 0.14 ± >0.01 wt %. A significant percentage of the high (22.8%) and medium (7.2%) limits within this subdivision are associated with the steep inner crater slopes.

Longitudinal and transverse geological sections through ellipse 1 show its model internal structure (Fig. 6). The material from ejecta accumulated in this

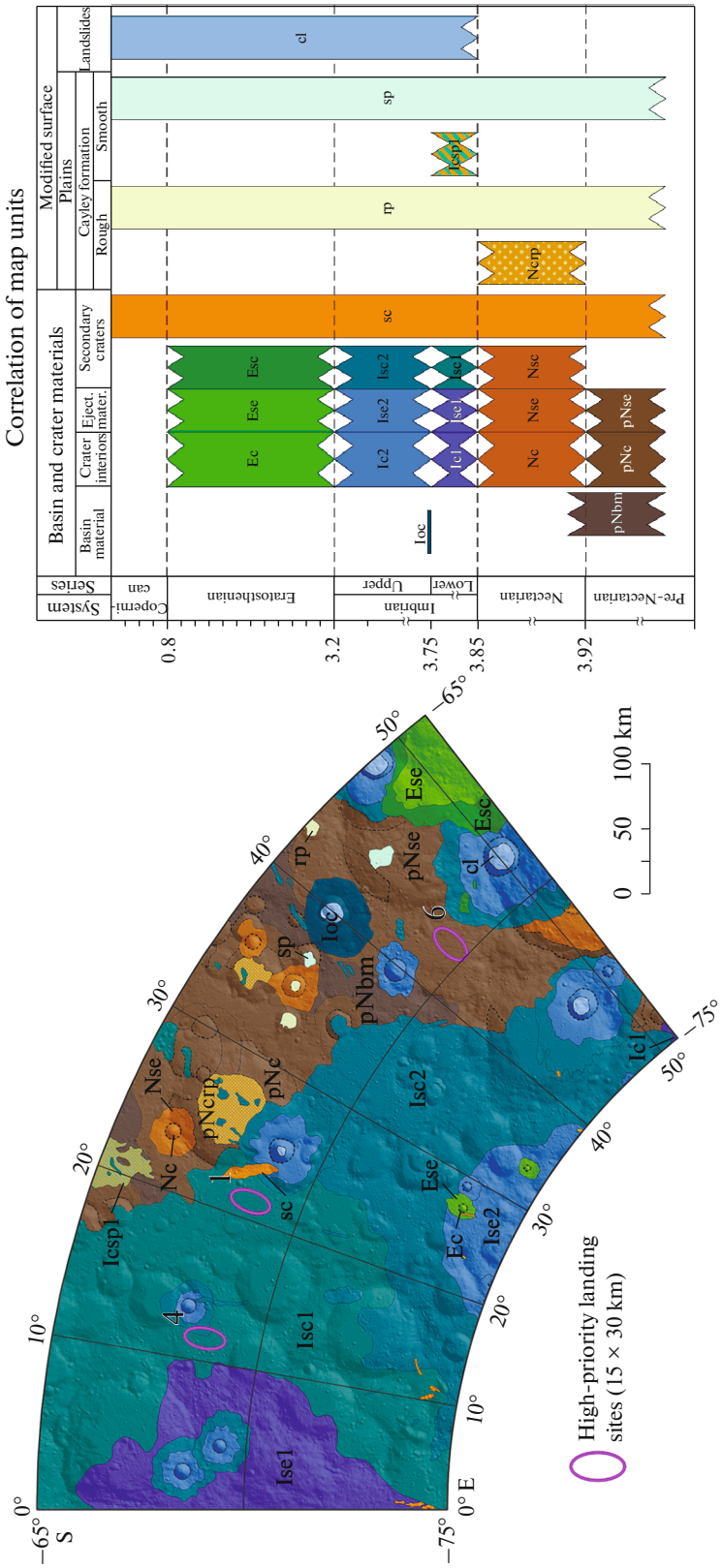

Fig. 2. Geological and geomorphological map (1 : 300000) of the *Luna-25* landing area.

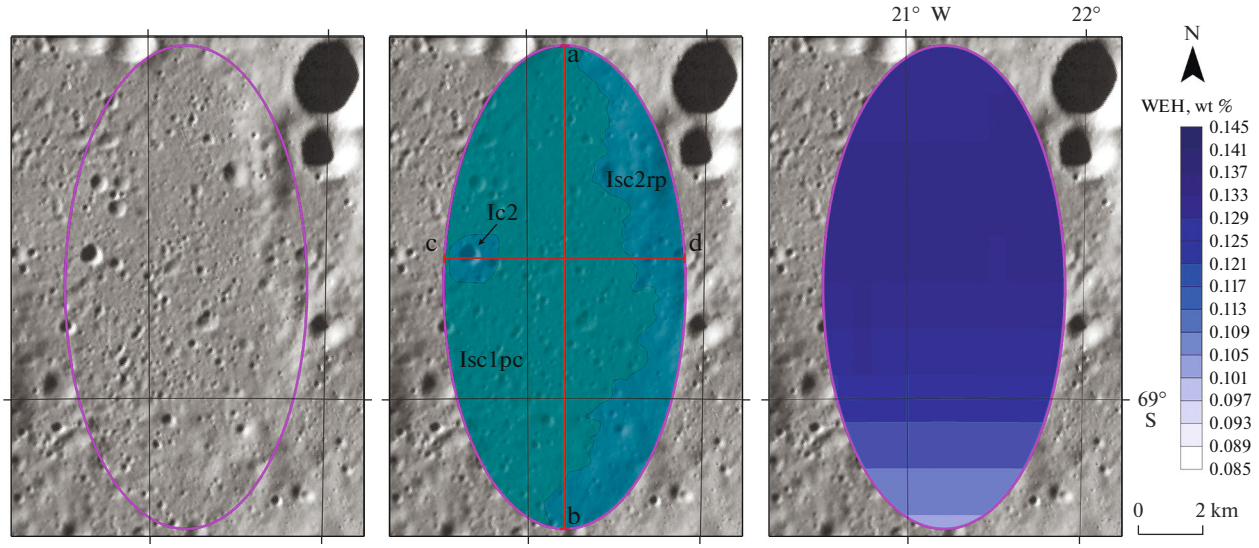

Fig. 3. Landing ellipse 1. Shown from left to right: surface morphology from WAC imagery, geological map of the ellipse (red lines show the position of geological sections, see (Fig. 6) and distribution of water equivalent hydrogen (WEH) abundance.

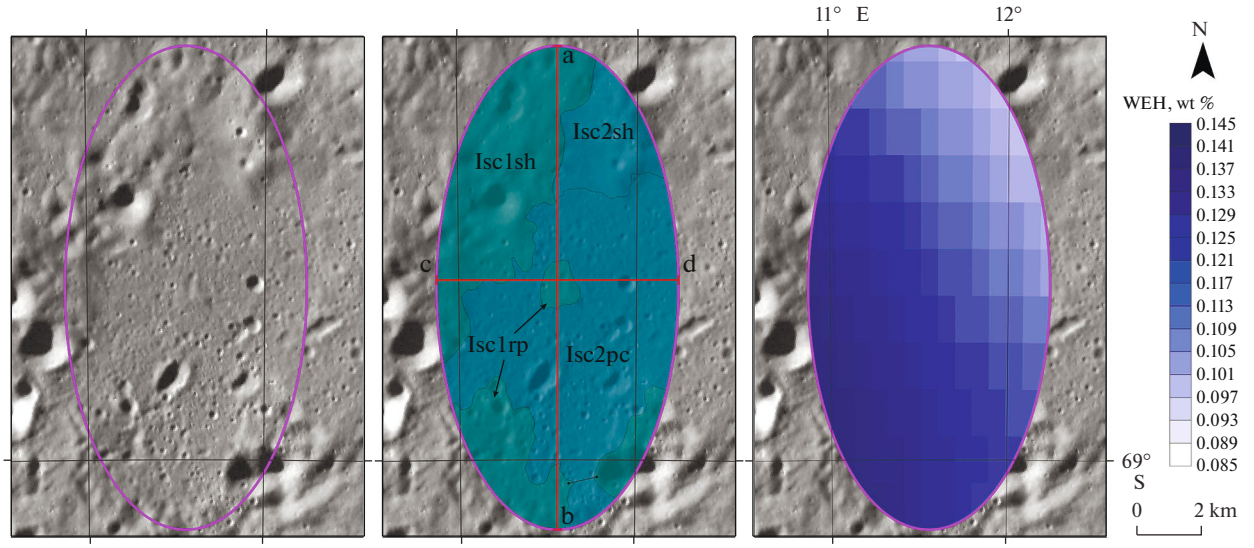

Fig. 4. Landing ellipse 4. Shown from left to right: surface morphology from WAC imagery, geological map of the ellipse (red lines show the position of geological sections, see (Fig. 6) and distribution of water equivalent hydrogen (WEH) abundance.

area lie predominantly subhorizontally. At the base of the sediments, there are ejecta from the SPA basin with an estimated thickness of about 870 m. They are overlain by ejecta from the Manzinus pre-Nectarian crater, which have a thickness of 180 to 85 m from N–E to S–W, respectively. Above, there are deposits of the crater Simpelius A (pNec) with a thickness of 35–18 m from S–W to N–E. On the surface itself, there are undifferentiated low-thickness deposits: from craters of pre-Nectarian age (Manzinus H with a thickness of 6 to 1 m from west to east, respectively; Manzinus D, 22–5 m, SE–N–W); Nectarian age (Manzinus C, 19–2 m, S–N) and Upper Imbrian age (Manzinus E, 2–1 m, E–W). The surface is complicated by a small number of small craters, the deposits of which are shown by the subscript (uc), but since the section does not always intersect these craters at the central point, the zone of their maximum excavation is shown with a dashed line (Fig. 6). The excavation depth of all the large craters presented, except for the craters Manzinus H (pNec) and Manzinus E (UpImb), is greater than the cover of the SPA sediments, and their ejecta may contain material that is older than in the SPA.

The proportion of surface slopes based on the first meters exceeding 10° and determined from the shadows in the NAC imagery is 26% (Krasilnikov et al.,

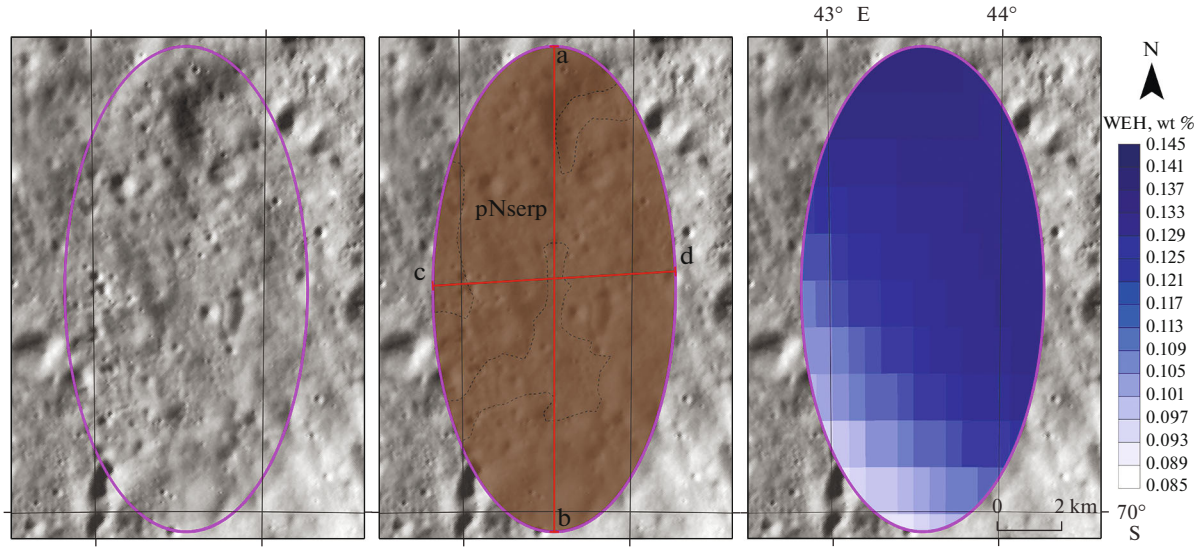

Fig. 5. Landing ellipse 6. Shown from left to right: surface morphology from WAC imagery, geological map of the ellipse (red lines show the position of geological sections, see (Fig. 6) and distribution of water equivalent hydrogen (WEH) abundance.

2018), and according to LOLA data on the base of 60 m, 4.15%. The sharp increase in the proportion of slopes is associated with the influence of small (the first tens of meters in diameter) craters with steep slopes (>7°). The average distance between such nearest craters in ellipse 1 for subdivision Isc2rp is ~23.3 ± 13.3 m, and for subdivision Isc1pc 14.2 ± 7.7 m (Ivanov et al., 2018).

Ellipse 4 (68.65° S, 11.55° E) has the most complex geological and geomorphological structure (Fig. 4). The ellipse is located on an intercrater plain composed of ejections from the Curtius, Simpelius E, and, presumably, from the Pentland A and Simpelius A craters of the Pre-Nectarian or Nectarian Age. Subsequently, the surface was covered by ejecta from the Lower Imbrian Moretus crater. Most of the ellipse is overlapped by ejecta from the Upper Imbrian age crater Pentland E, located on N-B outside the ellipse.

Within ellipse 4, four geological and geomorphological subdivisions are marked:

(1) The Lower Imbrian slightly sloping surface with hills and elongated depressions (Isc1sh, 27.7% of the ellipse surface) with an insignificant concentration of small craters is located in the northwest of the ellipse. The average WEH value for this unit is 0.12 ± 0.01 wt %. The surface area of this subdivision with high limits is 10.2%, and with medium limits it is 13.1%.

(2) The Lower Imbrian hilly-depression plain is characterized by elongated depressions of secondary impact craters (Isc1rp, 13.4% of the ellipse surface) and is located in the southern part of the ellipse. The absolute model age is ~3.82 ± 0.04 Ga (Ivanov et al., 2018); for them, there is an increase in the average WEH values up to 0.13 ± 0.01 wt %. The surface area of this subdivision with high limits is 15.5%, and with medium limits it is 12.8%.

(3) Located in the northeastern part of the ellipse, the Upper Imbrian surface with gentle hills (Isc2sh) was formed by the ejecta of the Pentland E crater, occupies 10% of the territory and has a low concentration of small craters. The absolute model age of the surface is estimated as ~3.6 ± 0.03 Ga (Ivanov et al., 2018). The WEH values are 0.1 ± 0.01 wt %. The surface area of this subdivision with high limits is 2.2%, and with medium limits it is 12%.

(4) Upper Imbrian cratered low undulating plain with a high concentration of small craters (Isc2pc, 48.9% of the territory). Presumably, the surface of this subdivision was formed by ejecta from the Pentland E crater and has an absolute model age of ~3.69 ± 0.03 Ga (Ivanov et al., 2018). The WEH values for this unit are 0.12 ± 0.01 wt %. The plain has a small area with high (4.5%) and medium (4.9%) limits.

Geological sections through the ellipse (Fig. 6) show that in its southeastern and central parts, the ejecta occur subhorizontally, and in the northwestern part, there is an uneven thickening of ejecta from the Curtius crater, due to which hills and depressions are formed on the surface. At the base of the sediments, there is SPA material with a thickness of about 850 m. Above the section, there are sediments of the Curtius pre-Nectarian crater, the thickness of which varies from 90 to 52 m in the NE–SW direction, while in the NW part of the ellipse the thickness deposits can double due to the uneven distribution of the ejected material. Above, there are deposits of the crater Simpelius E (pNec), the thickness of which decreases from 95 to 8 m in the S–N direction. Above, there are deposits of the crater Simpelius A (pNec) with a thickness of 48–21 m (SE–

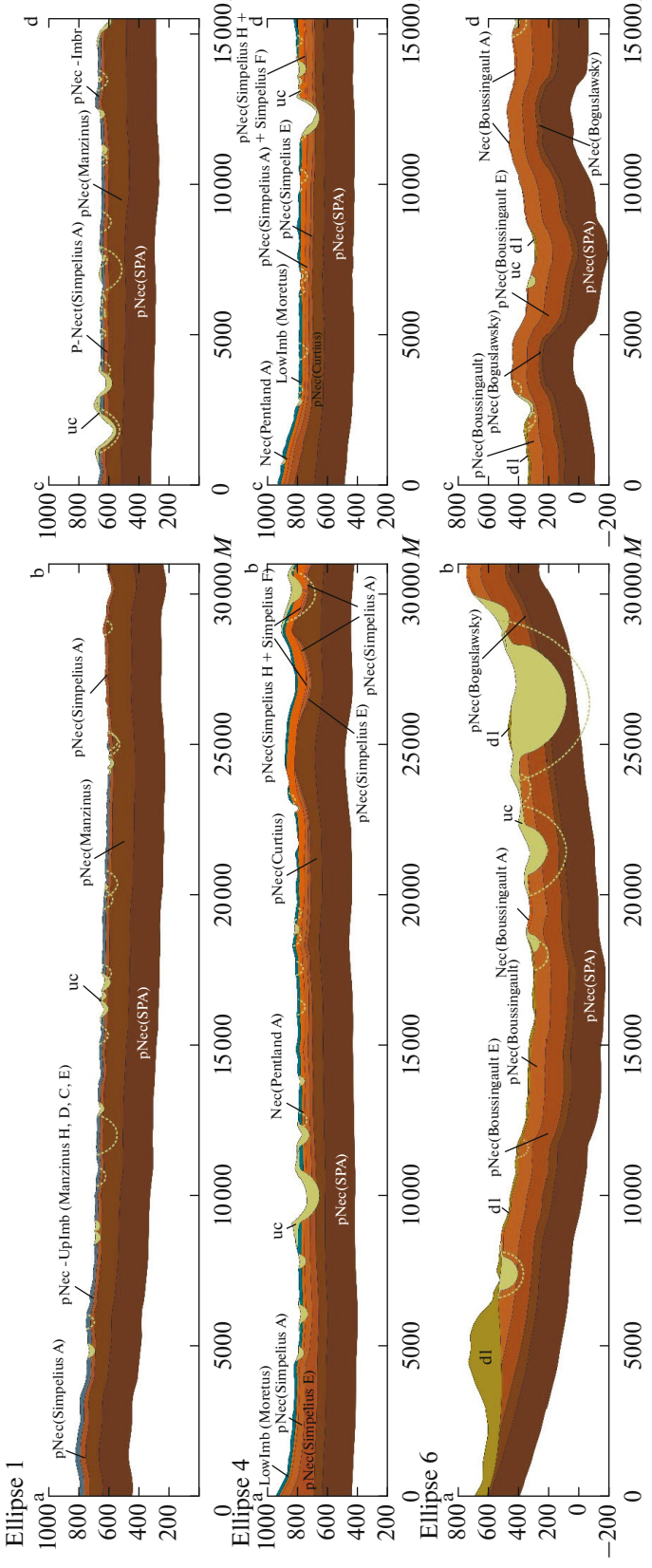

Fig. 6. Geological sections through landing ellipses 1, 4 and 6. The thickness of the largest craters/basins deposits is shown. Light green color shows the redistribution of deposits as a result of the formation of small craters (uc), as well as the area of their possible influence (dashed line). A landslide (dl) is shown within ellipse 6. The position of the cuts is shown in Figs. 3–5.

NW). At even higher horizons in the eastern part of the ellipse, deposits of the pre-Nectarian craters Simpelius H and Simpelius F can be encountered, which were not noted in the section due to their low thickness. Crater Pentland A (Nec) formed ejecta with a thickness of 63–10 m (NE–SW). The surface layer of the ellipse is formed by ejections from the Lower Imbrian crater Moretus with a thickness of 20 to 16 m in the SW–NE direction. The section is complicated by small elongated craters, presumably secondary, from the Moretus crater.

The proportion of slopes >10° based on several meters using the shadow method is 23% (Krasilnikov et al., 2018), and according to LOLA data, the slope value >10° is 6.34%. As in ellipse 1, the sharp increase in steep slopes is associated with a large number of small (first tens of meters) steep craters.

Ellipse 6 (69.55° S, 43.54° E) has a relatively homogeneous geological and geomorphological structure (Fig. 5). The ellipse is located between three large pre-Nectarian craters: Boguslawsky (~95 km in diameter), Boussingault (~128 km) and Boussingault E (~107 km). The surface of the ellipse is composed mainly of ejecta from the Boussingault crater and possibly from the neighboring craters Boussingault A (Nec), Boussingault K and Boussingault F (Ic2). In the hilly-depression plain of pre-Nectarian age with an average concentration of craters (pNserp), subdivisions of the second order can be distinguished: a hilly-depression slightly sloping surface with elongated relief forms (80.8% of the territory) and elongated depressions (19.2%) (Ivanov et al., 2018). Their absolute model age is ~4.04 ± 0.03 Ga (Ivanov et al., 2018). In the southern part of the ellipse, there is a landslide body with deposits of pre-Nectarian age (dl, Fig. 6). The WEH values gradually increase when moving from south to north and amount to about 0.14 wt %. The share of the territory with high limits is 7.2%, with medium limits, 12.1%.

At the base of the geological section of ellipse 6 (Fig. 6), there are SPA deposits with a thickness of about 1 km. The SPA deposits are overlain by ejecta from the Boguslawsky crater, the thickness of which varies from 74 to 32 m in the S–N direction. Above are the deposits of the crater Boussingault E (pNec) with a thickness of 152–95 m (N–E–S–W) and Boussingault (pNec) with a thickness of 210–85 m (E–W). The deposits of the Nectarian crater Boussingault A within the ellipse are probably fragmentary and have a thickness of 20–14 m. The thickness of the deposits of the youngest large craters Boussingault F (UpImb) and Boussingault K (UpImb) within the landing ellipse does not reach 2 m in total and, apparently, did not have a significant impact on the geological structure of the territory. These craters most likely pierced the cover of the SPA sediments and may contain older material in their ejecta. The surface of the ellipse is complicated by younger small craters of the Imbrian-Copernican age and a landslide in the southern part of the ellipse.

The proportion of surface slopes exceeding 10° on a 3.5 m base, according to the shadow method, is estimated as the smallest among the studied ellipses and amounts to 17% (Krasilnikov et al., 2018). According to LOLA, the area of the territory with a proportion of slopes >10° is 5.28% (Krasilnikov et al., 2021). The average distance between shaded small craters for pNserp is ~18.5 ± 10 m, for elongated depressions 18.4 ± 10.2 m (Ivanov et al., 2018).

LANDING SITE DETAILS AND CONCLUSIONS

Taking into account the spatial distribution of slopes on the basis of 60 m (Fig. 1), surface illumination by the Sun and visibility from the Earth within the area of the major landing ellipses with high (red area), medium (yellow), and low (green) engineering constraints on the landing and subsequent operation of the descent vehicle were identified (Fig. 7). For areas with low limits, all engineering requirements for the lander are met: surface illumination >45%, line of sight from the Earth 100%, and surface slopes <7°. Areas with average restrictions are characterized by the presence of one or several limiting factors with average indicators: the share of the average surface illumination is 40–45%, the share of visibility from the Earth is 95–99%, and the slopes on the surface are 7°–10°. Areas with high limits are characterized by surface slopes above critical (10°), a low proportion of the average surface illumination (≤40%), a low (≤95%) proportion of visibility from the Earth, or some of these parameters. High slope values are mainly associated with small craters, elongated ridges and troughs, indicating an uneven distribution of materials from nearby craters. For ellipses 1 and 4, small craters, however, can represent objects of high scientific importance, since they often penetrate the thin cover of the emissions of the Imbrian Age and could bring to the surface samples of the underlying layers of the Nectarian and Pre-Nectarian Ages.

Within ellipse 1, there are three geological and geomorphological subdivisions: (1) a relatively flat cratered plain of the Lower Imbrian Age (Isc1pc, occupying 70.5% of the territory), (2) a slightly sloping hilly-depression surface with elongated ridges and depressions of the Upper Imbrian Age (Isc2rp, 21.1%) and (3) an average crater with ejecta (Ic2, 8.4%). The most promising from a scientific point of view can be considered the northern part of the first subdivision (Isc1pc), where the average WEH values are 0.13 ± >0.01 wt %. The flat cratered plain of this subdivision is composed of ejecta from the crater Moretus of the Lower Imbrian Age (~3.82 ± 0.02 Ga) with a thickness of about 10 m. Further down the section, there are deposits of pre-Nectarian craters: Manzinus D (~30 km in diameter), Simpelius A (~58 km) and

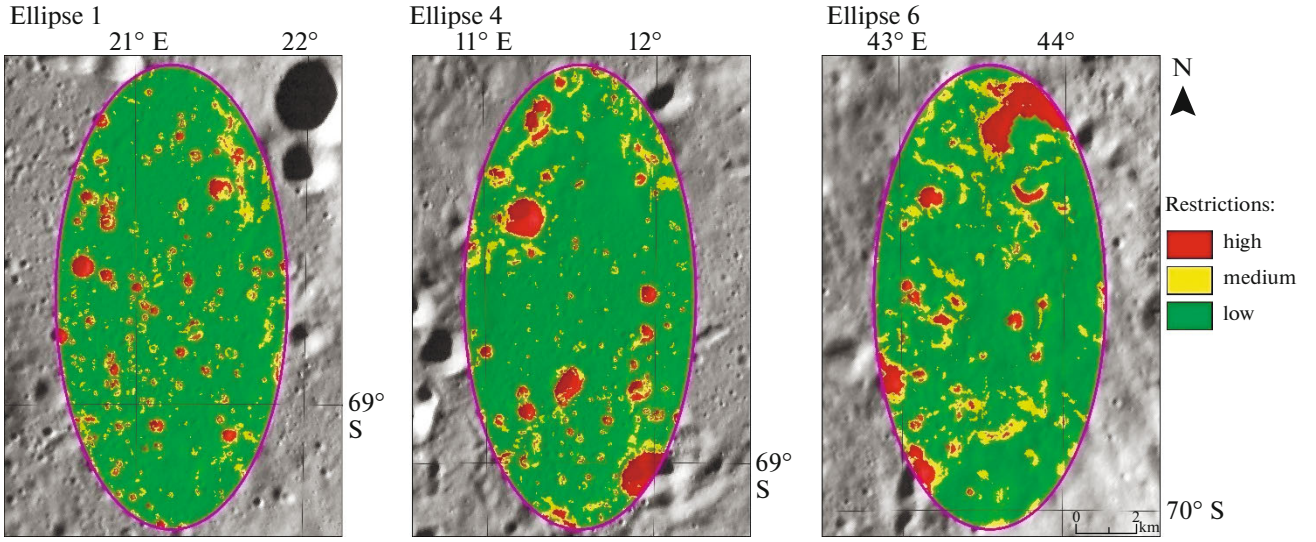

Fig. 7. Engineering and technical limitations for the landing and operation of the lander.

Manzinus crater (~94 km). The dimensions of these craters suggest that the excavation depth (usually taken equal to 1/10th of the crater diameter) was sufficient to eject material from under the SPA cover (model thickness 870 m) and, therefore, the SPA impact event prior to the impact event. This substance must belong to the very early stages of the formation of the lunar crust and is an object of extremely high scientific value.

Within ellipse 4, four geological and geomorphological subdivisions are marked: (1) a slightly sloping Lower Imbrian surface with hills and elongated depressions (Isc1sh, 27.7% of the ellipse surface), (2) a hilly-depression plain of the Lower Imbrian Age is characterized by elongated depressions of secondary impact craters (Isc1rp, 13.4%), (3) located in the northeastern parts of the ellipse Upper Imbrian surface with gentle hills (Isc2sh, 10%), (4) Upper Imbrian cratered weakly wavy plain with a high concentration of small craters (Isc2pc, 48.9%). Scientifically promising is a part of the Upper Imbrian (~3.69 ± 0.03 Ga) cratered plain (Isc2pc) with a high concentration of small craters in the western part of the ellipse (Fig. 7). The WEH values gradually increase towards the southwest of the ellipse and in this region reach 0.13 ± 0.01 wt %. In this area, under the thin (<5 m) Upper Imbrian deposits of the Pentland E crater (~11 km in diameter) are the Lower Umbrian deposits of the Moretus crater (~116 km), Pentland A (Nec, ~43 km), Simpelius A (pNec, ~58 km), Simpelius E (pNec, ~40 km), and Curtius (~95 km). The model SPA sediment thickness in this area is ~850 m. The ejections from these and small craters, ubiquitous within this area, should contain Nectarian and pre-Nectarian-Age material ejected from the surface sediments.

Ellipse 6 is located on a hilly-depression plain of the pre-Nectarian age with an average concentration of craters (pNserp) and has a homogeneous geological structure, but elongated depressions with higher slope values may be dangerous when landing. From a scientific point of view, the most promising can be considered the eastern part of the ellipse (Fig. 7), where the WEH values averaged 0.13 ± >0.01 wt %. The surface in this part of the ellipse is represented by a hilly-depressive plain of the pre-Nectarian age (~4.04 ± 0.03 Ga, subdivision pNserp), composed of ejecta from the Boussingault crater (pNse, ~129 km) with a model thickness of about 210 m. On the surface, a fragmentary presence of crater deposits is also possible. Boussingault A (Nec, ~75 km) with a thickness of up to 20 m. Down the section, there are deposits of Boussingault, Boussingault E (pNec, ~107 km) and the Boguslawsky crater (~95 km). The diameters of these craters are such that the excavation depth exceeds the model capacity of the SPA emissions, and their ejecta may contain samples of older rocks that precede the formation of the SPA basin.

FUNDING

The work was carried out with the financial support of the Russian Science Foundation grant no. 21-17-00035: Estimation of the rate of exogenous renewal of the lunar surface.

CONFLICT OF INTEREST

The authors declare that they have no conflicts of interest.

REFERENCES

Abdrakhimov, A.M., Basilevsky, A.T., Ivanov, M.A., Kokhanov, A.A., Karachevtseva, I.P., and Head, J.W., Occurrence probability of slopes on the lunar surface:

Estimate by the shaded area percentage in the LROC NAC images, *Sol. Syst. Res.,* 2015, vol. 49, no. 5, pp. 285–294. https://doi.org/10.7868/S0320930X15050011

Bandfield, J.L., Ghent, R.R., Vasavada, A.R., Paige, D.A., Lawrence, S.J., and Robinson, M.S., Lunar surface rock abundance and regolith fines temperatures derived from LRO diviner radiometer data, *J. Geophys. Res. E: Planets,* 2011, vol. 116, pp. 1–18. https://doi.org/10.1029/2011JE003866

Djachkova, M.V., Litvak, M.L., Mitrofanov, I.G., and Sanin, A.B., Selection of Luna-25 landing sites in the south polar region of the Moon, *Sol. Syst. Res.,* 2017, vol. 51, no. 3, pp. 185–195. https://doi.org/10.1134/S0038094617030029

Fassett, C.I., Head, J.W., Smith, D.E., Zuber, M.T., and Neumann, G.A., Thickness of proximal ejecta from the Orientale Basin from Lunar Orbiter Laser Altimeter (LOLA) data: Implications for multi-ring basin formation, *Geophys. Rev. Lett.,* 2011, vol. 38, p. L17201. https://doi.org/10.1029/2011GL048502

Hiesinger, H., van der Bogert, C.H., Pasckert, J.H., Schmedemann, N., Robinson, M.S., Jolliff, B., and Petro, N., New crater size-frequency distribution measurements of the South Pole–Aitken basin, *43th LPSC Conf.,* 2012, abs. 2863.

Housen, K.R., Schmidt, R.M., and Holsapple, K.A., Crater ejecta scaling laws: fundamental forms based on dimensional analysis, *J. Geophys. Res. B3,* 1983, vol. 88, pp. 2485–2499. https://doi.org/10.1029/JB088iB03p02485

Ivanov, M.A., Abdrakhimov, A.M., Basilevsky, A.T., Demidov, N.E., Guseva, E.N., Head, J.W., Hiesinger, H., Kohanov, A.A., and Krasilnikov, S.S., Geological characterization of the three high-priority landing sites for the Luna-Glob mission, *Planet. Space Sci.,* 2018, vol. 162, pp. 190–206. https://doi.org/10.1016/j.pss.2017.08.004

Krasilnikov, S.S., Basilevsky, A.T., Ivanov, M.A., Abdrakhimov, A.M., and Kokhanov, A.A., Steepness of slopes at the Luna-Glob landing sites: Estimating by the shaded area percentage in the LROC NAC images, *Sol. Syst. Res.,* 2018, vol. 52, no. 2, pp. 87–97. https://doi.org/10.1134/S0038094618010045

Krasilnikov, S.S., Basilevsky, A.T., Ivanov, M.A., and Krasilnikov, A.S., Geological and geomorphological characteristics of high-priority landing sites for the Luna-Glob mission, *Sol. Syst. Res.,* 2021, vol. 55, no. 2, pp. 83–96. https://doi.org/10.31857/S0320930X21010059

Mazarico, E., Neumann, G.A., Smith, D.E., Zuber, M.T., and Torrence, M.H., Illumination conditions of the lunar polar regions using LOLA topography, *Icarus,* 2011, vol. 211, pp. 1066–1081. https://doi.org/10.1016/J.ICARUS.2010.10.030

Paige, D.A., Foote, M.C., Greenhagen, B.T., Schofield, J.T., Calcutt, S., Vasavada, A.R., Preston, D.J., Taylor, F.W., Allen, C.C., Snook, K.J., Jakosky, B.M., Murray, B.C., Soderblom, L.A., Jau, B., Loring, S., Bulharowski, J., Bowles, N.E., Thomas, I.R., Sullivan, M.T., Avis, C., De Jong, E.M., Hartford, W., and McCleese, D.J., The Lunar Reconnaissance Orbiter Diviner lunar radiometer experiment, *Space Sci. Rev.,* 2010, vol. 150, pp. 125–160. https://doi.org/10.1007/s11214-009-9529-2

Robinson, M.S., Brylow, S.M., Tschimmel, M., Humm, D., Lawrence, S.J., Thomas, P.C., Denevi, B.W., Denevi, P.C., Bowman-Cisneros, E., Zerr, J., Ravine, M.A., Caplinger, M.A., Ghaemi, F.T., Schaffner, J.A., Malin, M.C., Mahanti, P., Bartels, A., Anderson, J., Tran, T.N., Eliason, E.M., McEwen, A.S., Turtle, E., Jolliff, B.L., and Hiesinger, H., Lunar Reconnaissance Orbiter Camera (LROC) instrument overview, *Space Sci. Rev.,* 2010, vol. 150, pp. 81–124. doi s11214-010-9634-2

Sanin, A.B., Mitrofanov, I.G., Litvak, M.L., Bakhtin, B.N., Bodnarik, J.G., Boynton, W.V., Chin, G., Evans, L.G., Harshman, K., Fedosov, F., Golovin, D.V., Kozyrev, A.S., Livengood, T.A., Malakhov, A.V., McClanahan, T.P., Mokrousov, M.I., Starr, R.D., Sagdeev, R.Z., Tret'yakov, V.I., and Vostrukhin, A.A., Hydrogen distribution in the lunar polar regions, *Icarus,* 2017, vol. 283, pp. 20–30. https://doi.org/10.1016/j.icarus.2016.06.002

Sharpton, V.L., Outcrops on lunar crater rims: implications for rim construction mechanisms, ejecta volumes and excavation depths, *J. Geophys. Res. E. Planets,* 2014, vol. 119, pp. 154–168. https://doi.org/10.1002/2013JE004523

Smith, D.E., Zuber, M.T., Jackson, G.B., Cavanaugh, J.F., Neumann, G.A., Riris, H., Xiaoli, S., Ronald, S.Z., Zellar, S., Coltharp, C., Connelly, J., Katz, R.B., Kleyner, I., Liiva, P., Matuszeski, A., Mazarico, E.M., McGarry, J.F., Novo-Gradac, A.-M., Ott, M.N., Peters, C., Ramos-Izquierdo, L.A., Ramsey, L., Rowlands, D.D., Schmidt, S., Stanley, V.S. III., Shaw, G.B., Smith, J.C., Swinski, J.-P., Torrence, M.H., Unger, G., Yu, A.W., and Zagwodzki, T.W., The lunar orbiter laser altimeter investigation on the Lunar Reconnaissance Orbiter mission, *Space Sci. Rev.,* 2010, vol. 150, pp. 209–241. https://doi.org/10.1007/s11214-009-9512-y

Wilhelms, D.E., Geologic mapping of the second planet, *US Geol. Surv. Interag. Report: Astrogeology,* 1972, vol. 55, pp. 199–238.